LETTERS
PUBLISHED ONLINE: 10 AUGUST 2014 | DOI: 10.1038/NNANO.2014.153
nature nanotechnology

Electrical control of a long-lived spin qubit in a Si/SiGe quantum dot

E. Kawakami[1‡], P. Scarlino[1‡], D. R. Ward[2], F. R. Braakman[1†], D. E. Savage[2], M. G. Lagally[2], Mark Friesen[2], S. N. Coppersmith[2], M. A. Eriksson[2] and L. M. K. Vandersypen[1*]

Nanofabricated quantum bits permit large-scale integration but usually suffer from short coherence times due to interactions with their solid-state environment[1]. The outstanding challenge is to engineer the environment so that it minimally affects the qubit, but still allows qubit control and scalability. Here, we demonstrate a long-lived single-electron spin qubit in a Si/SiGe quantum dot with all-electrical two-axis control. The spin is driven by resonant microwave electric fields in a transverse magnetic field gradient from a local micromagnet[2], and the spin state is read out in the single-shot mode[3]. Electron spin resonance occurs at two closely spaced frequencies, which we attribute to two valley states. Thanks to the weak hyperfine coupling in silicon, a Ramsey decay timescale of 1 µs is observed, almost two orders of magnitude longer than the intrinsic timescales in GaAs quantum dots[4,5], whereas gate operation times are comparable to those reported in GaAs[6–8]. The spin echo decay time is ~40 µs, both with one and four echo pulses, possibly limited by intervalley scattering. These advances strongly improve the prospects for quantum information processing based on quantum dots.

The proposal by Loss and DiVincenzo[9] to define quantum bits by the state of a single electron spin in a gate-defined semiconductor quantum dot has guided research for the past 15 years[7]. Most progress has been made with well-controlled III–V quantum dots, where spin manipulation with two[5,10], three[11] and four[12] dots has been realized, but gate fidelities and spin coherence times are limited by the unavoidable interaction with the fluctuating nuclear spins in the host substrate[4,5]. Although the randomness of the nuclear spin bath could be mitigated to some extent by feedback techniques[13], eliminating the nuclear spins by using group IV host materials offers the potential for extremely long electron spin coherence times. For instance, a dynamical decoupling decay time of half a second has been observed for an electron bound to a P impurity in ^{28}Si (ref. 14).

Much effort has been made to develop stable spin qubits in quantum dots defined in carbon nanotubes[15,16], Ge/Si core/shell nanowires[17], Si metal–oxide–semiconductor field-effect transistors (MOSFETs)[18,19] and Si/SiGe two-dimensional electron gases (2DEGs)[20–22]. However, coherent control in these group IV quantum dots is so far limited to a Si/SiGe singlet–triplet qubit with a spin dephasing time of 360 ns (ref. 22) and a carbon nanotube single-electron spin qubit, with a Hahn echo decay time of only 65 ns (ref. 15).

Our device is based on an undoped Si/SiGe heterostructure with two layers of electrostatic gates (Fig. 1a). Compared with conventional, doped heterostructures, this technology strongly improves charge stability[22]. First, accumulation gates ($V_a \approx +150$ mV) are used to induce a 2DEG in a 12-nm-wide Si quantum well 37 nm below the surface. Second, a set of depletion gates, labelled 1–12 in Fig. 1a, is used to form a single or double quantum dot in the 2DEG, flanked by a quantum point contact and another dot intended as charge sensors. Two 1-µm-wide, 200-nm-thick and 1.5-µm-long Co magnets are placed on top of the accumulation gates (Fig. 1a), providing a stray magnetic field with components $B_{||}$ and $B_{\perp}$, parallel and perpendicular to the external magnetic field, respectively. The sample is attached to the mixing chamber of a dilution refrigerator with base temperature ~25 mK, and the electron temperature estimated from transport measurements is ~150 mK. We tune the right dot to the few-electron regime (Supplementary Fig. 1c) and adjust the tunnel rate between the dot and the reservoir to ~1 kHz, so that dot–reservoir tunnel events can be monitored in real time using the sensing dot (Fig. 1a). The left dot is not used in the experiment and the constrictions between gates 4 and 8 and between 3 and 10 are pinched off. Gates 3, 8, 9 and 11 are connected to high-frequency lines via bias-tees. Microwave excitation applied to one of these gates oscillates the electron wavefunction back and forth in the dot. Because of the gradient $dB_{\perp}/dx \approx 0.3$ mT nm^{-1} (Fig. 1b), the electron is then subject to an oscillating magnetic field. Electric dipole spin resonance (EDSR) occurs when the microwave frequency f_{MW} matches the electron spin precession frequency in the magnetic field at the dot position[2,6].

All measurements shown here use four-stage voltage pulses applied to gate 3 (Fig. 1c): (1) initialization to spin-down (4 ms, fidelity of ~95%; Supplementary Section 7); (2) spin manipulation through microwave excitation of gate 8 (1 ms); (3) single-shot spin readout (4 ms, fidelity of ~95%; Supplementary Section 7); and (4) a compensation/empty stage (1 ms). By repeating this cycle, typically 150–1,000 times, we obtain statistics of how often an electron leaves the dot during the detection stage, giving the spin-up probability $P_{\uparrow}$ at the end of the manipulation stage. The measured spin resonance frequency as a function of applied magnetic field is shown in Fig. 2a. We can extract the electron g-factor using the relation

$$hf_0 = g\mu_B B_{local} \quad (1)$$

where $B_{local} = \sqrt{(B_{ext} + B_{||})^2 + B_{\perp}^2}$, h is Planck's constant, and μ_B is the Bohr magneton. From fits to equation (1) (blue curve in Fig. 2a), we find $g = 1.998 \pm 0.002$, where we used $B_{||} = 120$ mT and $B_{\perp} = 50$ mT, based on numerical simulation of the stray magnetic field from the micromagnet at the estimated dot location (Supplementary Section 2).

[1]Kavli Institute of Nanoscience, TU Delft, Lorentzweg 1, 2628 CJ Delft, The Netherlands, [2]University of Wisconsin-Madison, Madison, Wisconsin 53706, USA; [†]Present address: Department of Physics, University of Basel, 4056 Basel, Switzerland; [‡]These authors contributed equally to this work.
*e-mail: l.m.k.vandersypen@tudelft.nl

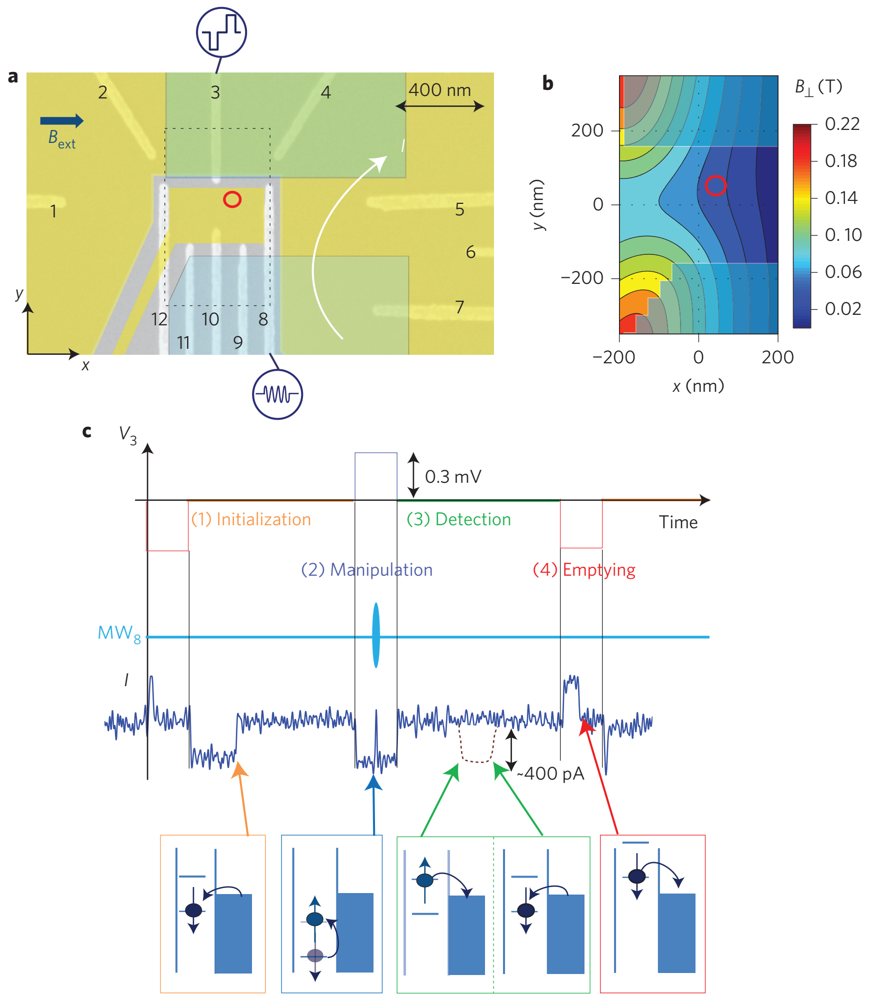

Figure 1 | Device schematic and measurement cycle. a, False-colour device image showing a fabricated pattern of split gates, labelled 1–12. For this experiment we create a single quantum dot (estimated location indicated by a red circle) and a sensing dot. Current I is measured as a function of time for a fixed voltage bias of −600 μeV. The voltage pulses are applied to gate 3 and the microwaves are applied to gate 8. Green semitransparent rectangles show the position of two 200-nm-thick Co micromagnets. The yellow-shaded areas show the location of two accumulation gates, one for the reservoirs and another for the double quantum dot region. **b**, Numerically computed magnetic field component perpendicular to the external field, induced by the micromagnet in the plane of the Si quantum well, for fully magnetized micromagnets. Straight solid lines indicate the edges of the micromagnet as simulated. The region shown is outlined with dotted lines in **a**. **c**, Microwave (MW) and gate voltage pulse scheme (see main text) as well as an example trace of I_{SD} recorded during the pulse cycle and cartoons illustrating the dot alignment and tunnel events. During stages (1) and (3) the Fermi level in the reservoir is set between the spin-down and spin-up energy levels so that only a spin-down electron can tunnel into the dot and only a spin-up electron can tunnel out[3]. During stage (2), the dot is pulsed deep into the Coulomb blockade to minimize photon-assisted tunnelling. The MW burst of duration t_p ends ~100–500 μs before the detection stage. When a step is observed during stage (3) (see the dotted line) we count the electron as spin-up. Stage (4) serves to keep the d. c. component of the pulse zero and to symmetrize pulse distortions from the bias-tee. In the process, the quantum dot is emptied. The spike during the manipulation stage is due to the influence of the microwave burst (here 700 μs) on the detector.

Surprisingly, when measuring the EDSR peak at a sufficiently low power to avoid power broadening, we resolve two lines, separated by 2–4 MHz in the range $B_{ext} = 0.55$–1.2 T (Fig. 2b). We return to the origin of this splitting later. Fitting each resonance peak with a Gaussian function yields $\delta f^{(2)}_{FWHM} = 0.63 \pm 0.06$ MHz for the higher-energy transition at frequency $f^{(2)}_0$ and $\delta f^{(1)}_{FWHM} = 0.59 \pm 0.05$ MHz for the lower-energy transition at frequency $f^{(1)}_0$. From this linewidth we extract a dephasing time

$$T_2^* = \frac{\sqrt{2}\hbar}{g\mu_B\sigma_B} = \frac{2\sqrt{\ln 2}}{\pi\delta f_{FWHM}} = 840 \pm 70\ \text{ns}$$

(ref. 7), 30–100 times longer than T_2^* in III–V dots[4,5,7,8]. This dephasing timescale can be attributed to the random nuclear field from the 5% ^{29}Si atoms in the substrate with standard deviation $\sigma_B = 9.6$ μT, consistent with theory[23]. Previous T_2^* measurements in Si/SiGe dots[22,24] gave somewhat shorter values of 220–360 ns. T_2^* is expected to scale with the square root of the number of nuclear spins with which the electron wavefunction overlaps. Considering these other measurements were done on double dots, this would imply variations in the volume per dot up to a factor of 7, if nuclear spins were dominating the decay. Given the presence of a magnetic field gradient $dB_{||}/dx \approx 0.2$ mT nm^{-1}, the linewidth also gives an upper bound on the electron micromotion induced by low-frequency charge noise of ~50 pm (r.m.s.).

Coherent control of the electron spin is achieved by applying short high-power microwave bursts of duration t_p. Figure 3a shows the measured spin-up probability, $P_\uparrow$, as a function of f_{MW} and burst time t_p, which exhibits the chevron pattern that is

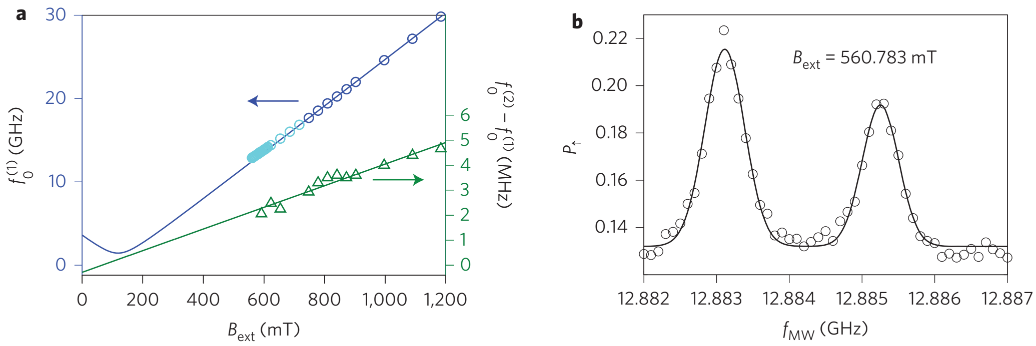

Figure 2 | Qubit spectroscopy. a, Measured microwave frequency that matches the electric dipole spin resonance condition $f_0^{(1)}$ (dark blue and light blue circles) and the difference between the two resonance frequencies $f_0^{(2)} - f_0^{(1)}$ (green triangles) as a function of externally applied magnetic field. The six points where $f_{MW} > 20$ GHz are measured by two-photon transitions[25]. The microwave burst time $t_p = 700\ \mu s \gg T_2^*$, effectively corresponding to continuous-wave (c.w.) excitation (here we used low-power excitation, $P = -33$ dBm to -10 dBm at the source, decreasing with lower microwave frequency). The upper of the two resonances in **b** is shown. The blue solid curve is a fit to the dark blue circles using equation (1). Light blue circles are excluded from the fit; presumably the micromagnet begins to demagnetize here. The green line is a linear fit to the green triangles. **b**, Measured spin-up probability $P_\uparrow$ as a function of applied microwave frequency f_{MW} for $B_{ext} = 560.783$ mT ($P = -33$ dBm), averaged over 200 min (that is, 1,200,000 single-shot measurements).

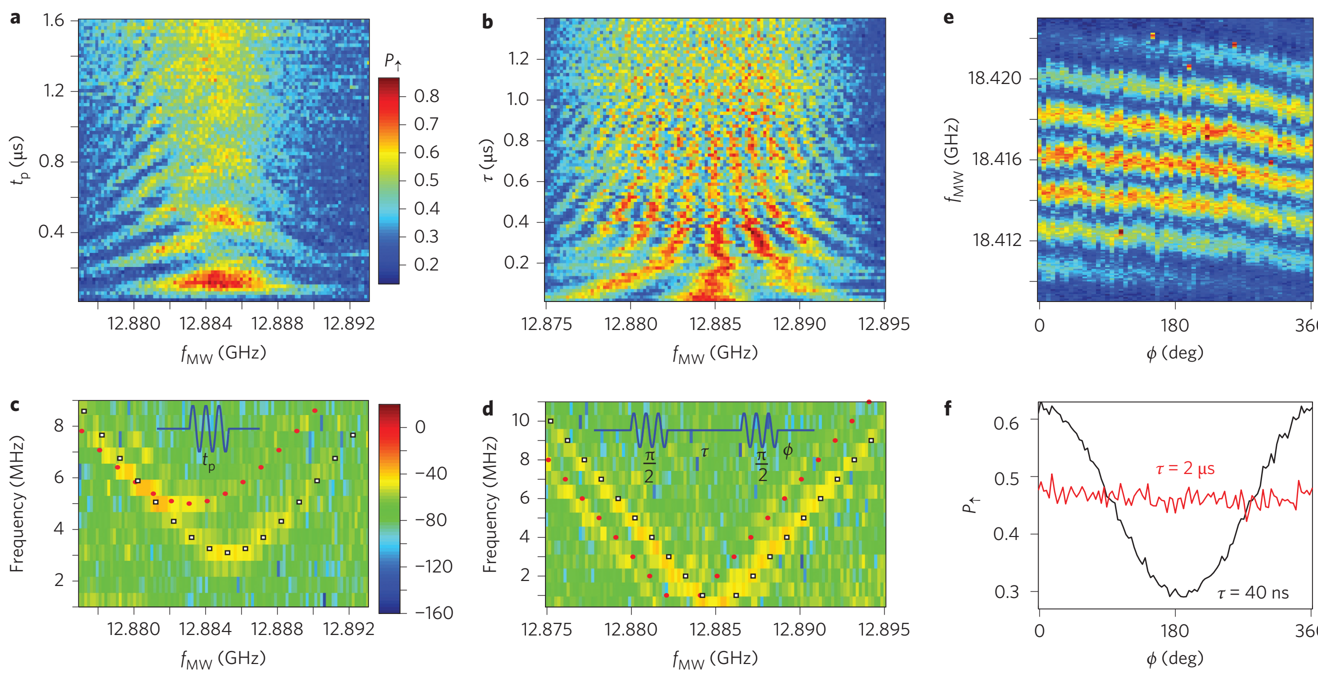

Figure 3 | Universal qubit control. a, Measured spin-up probability, $P_\uparrow$, as a function of f_{MW} and burst time t_p ($B_{ext} = 560.783$ mT, $P = 16.4$ dBm). **b**, Measured spin-up probability, $P_\uparrow$, as a function of f_{MW} and waiting time τ ($B_{ext} = 560.783$ mT, $P = 16.4$ dBm) between two $\pi/2$ (75 ns) pulses with equal phase, showing Ramsey interference. Colour map as in **a**. **c**, Fourier transform over the microwave burst time t_p of **a**, showing a hyperbolic dependence (black rectangles and red circles) as a function of f_{MW} for each transition, $f_0^{(1)}$ and $f_0^{(2)}$. Inset: Microwave pulse scheme used in **a**,**c**. **d**, Fourier transform over the waiting time τ of **b** showing two linear patterns superimposed, with vertices at $f_0^{(1)}$ and $f_0^{(2)}$. Inset: Microwave pulse scheme used in **b**,**d**–**f**. Colour map as in **c**. **e**, Measured spin-up probability, $P_\uparrow$, as a function of f_{MW} and the relative phase ϕ between two microwave pulses for $\tau = 400$ ns ($B_{ext} = 763.287$ mT, $P = 18.8$ dBm). Colour map as in **a**. **f**, Ramsey signal as a function of the relative phase ϕ between the two microwave pulses for $\tau = 40$ ns (black curves) and $\tau = 2\ \mu s$ (red curves). $B_{ext} = 763.287$ mT, $P = 18.8$ dBm, $f_{MW} = f_0^{(2)} = 18.41608$ GHz.

characteristic of high-quality oscillations (here two partly overlapping patterns). On resonance, the spin rotates at the bare Rabi frequency, f_1. When detuned away from resonance by $\Delta f = f_{MW} - f_0$, the spin rotates about a tilted axis, the oscillation frequency increases as $\sqrt{\Delta f^2 + f_1^2}$, and the visibility is reduced. The fast Fourier transform (FFT) over the microwave burst time of the data in Fig. 3a is shown in Fig. 3c and exhibits the expected hyperbolic dependence as a function of Δf for both transitions, $f_0^{(1)}$ and $f_0^{(2)}$. We fit both hyperbolae with one free parameter f_1 each (Figs 3c,d, black rectangles and red circles), giving $f_1^{(1)} = 5.0 \pm 0.6$ MHz ($B_1 \approx 0.18$ mT) and $f_1^{(2)} = 3.1 \pm 0.6$ MHz (errors arise from the finite number of points in the FFT) for the respective transitions. These single-spin Rabi frequencies are comparable to those observed in GaAs[6,8]. The relative amplitude of the oscillations at $f_0^{(1)}$ and $f_0^{(2)}$ is ~30/70; note that, despite its lower weight, the peak at $f_0^{(1)}$ is tallest in Fig. 2b, because its Rabi frequency is a factor of 1.5 ± 0.2 higher than that of the other peak (Supplementary Section 5). The extracted Rabi frequencies of both transitions are proportional to the microwave amplitude, as expected (Supplementary Fig. 5).

The observed decay of the Rabi oscillations cannot be explained only by the spread in the Larmor frequency, σ_B. Numerical simulations of the Rabi oscillations give good agreement with the measurements in Fig. 3a when including a variation in the Rabi frequency, $\sigma_{Rabi} \approx 0.25$ MHz (Supplementary Section 4). The fluctuations in the transverse nuclear field[25] are too small to explain this spread. Instead, instrumentation noise could be responsible. Modelling the gate operation taking into account f_1, σ_B and σ_{Rabi}, we estimate that the fidelity for flipping a spin from down to up is 0.99 (0.97) for an electron spin resonant at $f_1^{(1)}$ ($f_1^{(2)}$). For an electron in a 30/70 statistical mixture of the two resonance conditions, the fidelity is ~0.80 (Supplementary Section 7).

Two-axis control of the spin is demonstrated by varying the relative phase ϕ of two $\pi/2$ microwave bursts resonant with $f_1^{(2)}$ separated by a fixed waiting time $\tau = 40\,\text{ns} \ll T_2^*$ (Fig. 3f, black trace). As expected, the signal oscillates sinusoidally in ϕ with period 2π. For $\tau = 2\,\mu\text{s} > T_2^*$, the contrast has vanished, indicating that all phase information is lost during the waiting time (Fig. 3f, red trace). Similar measurements with the pulses applied off-resonance by an amount Δf with $\phi = 0$ are expected to show an oscillation with frequency Δf and an envelope that decays on the timescale T_2^*. Because of the presence of two resonance lines just 2.1 MHz apart, the measurement of $P_\uparrow$ versus f_{MW} and τ (Fig. 3b) shows a superposition of two such patterns. This becomes clear from taking the Fourier transform over the waiting time τ (Fig. 3d), which shows two linear patterns superimposed, with vertices at $f_0^{(1)}$ and $f_0^{(2)}$. The stability of the measurement can be appreciated from Fig. 3e, which shows $P_\uparrow$ versus f_{MW} and the relative phase between the two bursts at $\tau = 400$ ns.

Spin coherence can be extended by spin echo techniques, provided the source of dephasing fluctuates slowly on the timescale of the electron spin dynamics. We performed a Hahn echo experiment, consisting of $\pi/2$, π and $\pi/2$ pulses separated by waiting times $\tau/2$ (refs 7, 20), and recorded $P_\uparrow$ as a function of the total free evolution time τ (Fig. 4a). A fit to a single exponential yields a time constant $T_2 = 37 \pm 3\,\mu$s, almost 50 times longer than T_2^*. Although this is encouraging, we had expected an even longer T_2 based on the 200 μs Hahn echo decay observed for an electron spin bound to a P impurity in natural Si (ref. 26). Furthermore, contrary to our expectations for an echo decay dominated by slowly fluctuating nuclear spins, the decay is well-described by a single exponential, with no signatures of a flat top. One possible explanation is that the fluctuations that dominate the echo decay are fast compared with the few-microsecond timescale of the first few data points[27]. Another possible explanation is that the observed decoherence rate $1/T_2$ reflects the valley switching rate; as soon as the valley switches, the spin resonance frequency jumps by ~2 MHz, and the phase of the spin is randomized. Both explanations are consistent with the fact that a four-pulse decoupling pulse sequence does not further extend the decay time (Fig. 4b). Either way, this implies that the slowly fluctuating nuclear field does not yet limit T_2 (ref. 28). Finally, when we shift the position of the third pulse, the time intervals before and after the echo pulse are no longer equal and coherence is lost, as expected (Fig. 4c). A fit of this decay with a Gaussian function gives $T_2^* = 920 \pm 70$ ns measured in the time domain, consistent with T_2^* extracted from the linewidth.

We now return to the origin of the two resonance lines that are visible in all the measurements. From the individual measurements, we deduce that the higher (lower) frequency resonance contributes to the signal 70% (30%) of the time, indicating that the system does not simply exhibit two resonances but instead switches between two conditions. The splitting between the two lines varies linearly with B_{ext}, corresponding to a difference in g-factors of ~0.015%, and an offset in B_{local} between the two resonances of 65 ± 138 mT (Fig. 2a, green triangles). Finally, as mentioned before, the higher-frequency resonance exhibits ~1.5 times slower Rabi oscillations than the lower-frequency resonance.

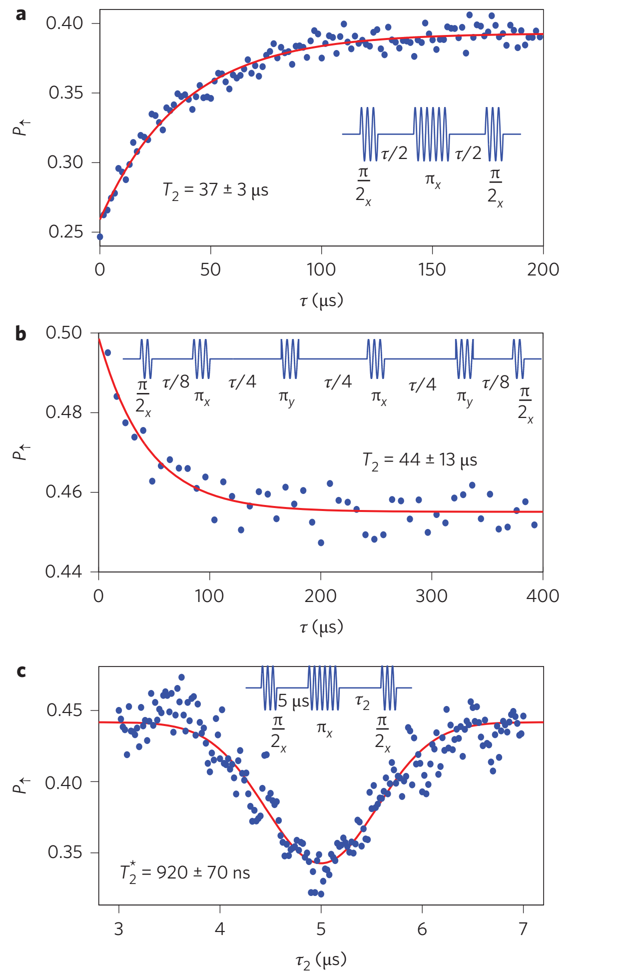

Figure 4 | Qubit coherence. **a**, Measured spin-up probability as a function of the total free evolution time τ in a Hahn echo experiment (pulse scheme shown in inset). A significant difference in the decay was not observed when changing the relative phase between the first pulse (77 ns) and the π pulse (150 ns) from $\phi = 0$ to $\phi = 90$. The decay curve is fit well to a single exponential decay. **b**, Measured spin-up probability as a function of the total free evolution time τ when using four decoupling pulses. **c**, Measured spin-up probability as a function of the position of the third pulse in the Hahn echo experiment. The free evolution time between the first and second pulses is fixed at 5 μs and that between the second and third pulses is varied from 3 to 7 μs. $B_{ext} = 747.710$ mT, $P = 18.4$ dBm, $f_{MW} = f_0^{(2)} = 17.695$ GHz; $f_1^{(2)} = 2.7$ MHz.

We propose that the two lines correspond to EDSR with the electron in one or the other of the two lowest valley states, with a 30/70 occupation ratio. This ratio is set either by the injection probabilities into the respective valley states, or by thermal equilibration, depending on whether the valley lifetime is shorter than the few-millisecond delay between injection and manipulation. We note that, either way, initialization to a single valley can be achieved when the valley splitting is several times larger than the electron temperature. Initial reports of electric-field-controlled valley splittings in Si dots may point to a way of achieving such control[18]. A valley-dependent spin splitting can arise from several sources. Intrinsic spin–orbit coupling is weak in silicon, but the field gradient from the micromagnet admixes spin and orbitals, leading to a renormalization of the g-factor by an amount that depends on the orbital level spacing[2]. Due to valley–orbit coupling, the orbital level spacing in turn depends on the valley. We estimate that this can result in observed valley-dependent g-factor shifts of ~0.015% (Supplementary Section 10). The difference in Rabi frequencies can also be understood from a valley-dependent orbital level spacing. Another mechanism that can account for the observed g-factor shifts is valley-dependent penetration of the Bloch wavefunction into the SiGe barrier region (Supplementary Section 10). Other explanations we considered include switching between two separate dot locations, a double dot and transitions in a two-electron manifold, but these are not consistent with the above observations (see Supplementary Information).

The demonstration of all-electrical single-spin control with coherence times orders of magnitude longer than intrinsic coherence timescales in III–V hosts greatly enhances the promise of quantum-dot-based quantum computation. The presence of two closely spaced resonances that we attribute to occupation of two different valleys shows the necessity for valley splitting control[18], not only for exchange-based quantum gates[20], but also for single-spin manipulation. The use of a micromagnet facilitates selective addressing of neighbouring spins and provides a coupling mechanism of quantum dot spins to stripline resonators that can form the basis for two-qubit gates and a scalable architecture[29].

Received 26 February 2014; accepted 27 June 2014; published online 10 August 2014

References

1. Eckstein, J. N. & Levy, J. Materials issues for quantum computation. *Mater. Res. Soc. Bull.* **38,** 783–789 (2013).
2. Tokura, Y., Van der Wiel, W. G., Obata, T. & Tarucha, S. Coherent single electron spin control in a slanting Zeeman field. *Phys. Rev. Lett.* **96,** 047202 (2006).
3. Elzerman, J. M. *et al.* Single-shot read-out of an individual electron spin in a quantum dot. *Nature* **430,** 431–435 (2004).
4. Chekhovich, E. A. *et al.* Nuclear spin effects in semiconductor quantum dots. *Nature Mater.* **12,** 494–504 (2013).
5. Petta, J. R. *et al.* Coherent manipulation of coupled electron spins in semiconductor quantum dots. *Science* **309,** 2180–2184 (2005).
6. Obata, T. *et al.* Coherent manipulation of individual electron spin in a double quantum dot integrated with a micromagnet. *Phys. Rev. B* **81,** 085317 (2010).
7. Hanson, R., Kouwenhoven, L. P., Petta, J. R., Tarucha, S. & Vandersypen, L. M. K. Spins in few-electron quantum dots. *Rev. Mod. Phys.* **79,** 1217–1265 (2007).
8. Koppens, F. H. L. *et al.* Driven coherent oscillations of a single electron spin in a quantum dot. *Nature* **442,** 766–771 (2006).
9. Loss, D. & DiVincenzo, D. P. Quantum computation with quantum dots. *Phys. Rev. A* **57,** 120 (1998).
10. Nowack, K. C. *et al.* Single-shot correlations and two-qubit gate of solid-state spins. *Science* **333,** 1269–1272 (2011).
11. Medford, J. *et al.* Self-consistent measurement and state tomography of an exchange-only spin qubit. *Nature Nanotech.* **8,** 654–659 (2013).
12. Shulman, M. D. *et al.* Demonstration of entanglement of electrostatically coupled singlet–triplet qubits. *Science* **336,** 202–205 (2012).
13. Bluhm, H., Foletti, S., Mahalu, D., Umansky, V. & Yacoby, A. Enhancing the coherence of a spin qubit by operating it as a feedback loop that controls its nuclear spin bath. *Phys. Rev. Lett.* **105,** 216803 (2010).
14. Muhonen, J. T. *et al.* Storing quantum information for 30 seconds in a nanoelectronic device. Preprint at http://arxiv.org/abs/1402.7140v1 (2014).
15. Laird, E. A., Pei, F. & Kouwenhoven, L. P. A valley–spin qubit in a carbon nanotube. *Nature Nanotech.* **8,** 565–568 (2013).
16. Churchill, H. O. H. *et al.* Electron–nuclear interaction in ^{13}C nanotube double quantum dots. *Nature Phys.* **5,** 321–326 (2009).
17. Higginbotham, A. P. *et al.* Hole spin coherence in a Ge–Si heterostructure nanowire. *Nano Lett.* **14,** 3582 (2014).
18. Yang, C. H. *et al.* Spin–valley lifetimes in a silicon quantum dot with tunable valley splitting. *Nature Commun.* **4,** 2069 (2013).
19. Hao, X., Ruskov, R., Xiao, M., Tahan, C. & Jiang, H. Electron spin resonance and spin–valley physics in a silicon double quantum dot. *Nature Commun.* **5,** 3860 (2014).
20. Zwanenburg, F. A. *et al.* Silicon quantum electronics. *Rev. Mod. Phys.* **85,** 961 (2013).
21. Prance, J. R. *et al.* Single-shot measurement of triplet–singlet relaxation in a Si/SiGe double quantum dot. *Phys. Rev. Lett.* **108,** 046808 (2012).
22. Maune, B. M. *et al.* Coherent singlet–triplet oscillations in a silicon-based double quantum dot. *Nature* **481,** 344–347 (2012).
23. Assali, L. V. C. *et al.* Hyperfine interactions in silicon quantum dots. *Phys. Rev. B* **83,** 165301 (2011).
24. Wu, X. *et al.* Two-axis control of a singlet–triplet qubit with an integrated micromagnet. Preprint at http://arxiv.org/abs/1403.0019v1 (2014).
25. Laird, E. A. *et al.* A new mechanism of electric dipole spin resonance: hyperfine coupling in quantum dots. *Semicond. Sci. Technol.* **24,** 064004 (2009).
26. Pla, J. J. *et al.* A single-atom electron spin qubit in silicon. *Nature* **489,** 541–545 (2012).
27. Cywiński, Ł., Lutchyn, R. M., Nave, C. P. & Das Sarma, S. How to enhance dephasing time in superconducting qubits. *Phys. Rev. B* **77,** 174509 (2008).
28. Witzel, W. M. & Das Sarma, S. Quantum theory for electron spin decoherence induced by nuclear spin dynamics in semiconductor quantum computer architectures: spectral diffusion of localized electron spins in the nuclear solid-state environment. *Phys. Rev. B* **74,** 035322 (2006).
29. Xiang, Z. L., Ashhab, S., You, J. Q. & Nori, F. Hybrid quantum circuits: superconducting circuits interacting with other quantum systems. *Rev. Mod. Phys.* **85,** 623–653 (2013).

Acknowledgements

The authors acknowledge useful discussions with L. Schreiber, J. Prance, G. de Lange, A. Morello, W. Coish, F. Beaudoin and our spin qubit teams, comments by L. DiCarlo and R. Hanson, and experimental assistance from P. Barthelemy, M. Tiggelman and R. Schouten. This work was supported in part by the Army Research Office (ARO) (W911NF-12-0607), the Foundation for Fundamental Research on Matter (FOM) and the European Research Council (ERC). Development and maintenance of the growth facilities used for fabricating samples was supported by the Department of Energy (DOE) (DE-FG02-03ER46028). E.K. was supported by a fellowship from the Nakajima Foundation. This research utilized NSF-supported shared facilities at the University of Wisconsin–Madison.

Author contributions

E.K. and P.S performed the experiment with help from F.R.B., and analysed the data. D.R.W. fabricated the sample. D.E.S and M.G.L. grew the heterostructure. E.K., P.S., M.F., S.N.C., M.A.E. and L.M.K.V. carried out the interpretation of the data, and M.F and S.N.C. the theoretical analysis. E.K., P.S. and L.M.K.V. wrote the manuscript and all authors commented on the manuscript. M.A.E. and L.M.K.V. initiated the project, and supervised the work with S.N.C.

Additional information

Supplementary information is available in the online version of the paper. Reprints and permissions information is available online at www.nature.com/reprints. Correspondence and requests for materials should be addressed to L.M.K.V.

Competing financial interests

The authors declare no competing financial interests.